Journal Pre-proof

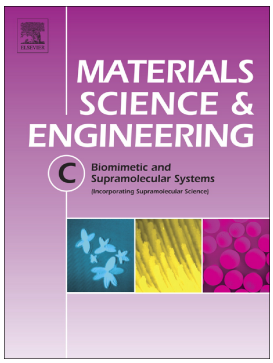

Addition of Sn to TiNb alloys to improve mechanical performance and surface properties conducive to enhanced cell activity

C. Torres-Sánchez, J. Wang, M. Norrito, L. Zani, P.P. Conway

PII: S0928-4931(19)34411-X

DOI: https://doi.org/10.1016/j.msec.2020.110839

Reference: MSC 110839

To appear in: *Materials Science & Engineering C*

Received date: 25 November 2019

Revised date: 19 February 2020

Accepted date: 11 March 2020

Please cite this article as: C. Torres-Sánchez, J. Wang, M. Norrito, et al., Addition of Sn to TiNb alloys to improve mechanical performance and surface properties conducive to enhanced cell activity, *Materials Science & Engineering C* (2020), https://doi.org/10.1016/j.msec.2020.110839

This is a PDF file of an article that has undergone enhancements after acceptance, such as the addition of a cover page and metadata, and formatting for readability, but it is not yet the definitive version of record. This version will undergo additional copyediting, typesetting and review before it is published in its final form, but we are providing this version to give early visibility of the article. Please note that, during the production process, errors may be discovered which could affect the content, and all legal disclaimers that apply to the journal pertain.

© 2020 Published by Elsevier.

Journal Pre-proof

Addition of Sn to TiNb alloys to improve mechanical performance and surface properties conducive to enhanced cell activity

C. Torres-Sánchez[1], J. Wang, M. Norrito, L. Zani, P.P. Conway

Wolfson School of Mechanical, Electrical and Manufacturing Engineering, Loughborough University, LE11 3TU, UK

Abstract

Titanium (Ti) alloys with Niobium (Nb) and Tin (Sn) were prepared in order to conduct a systematic study on the bulk and surface properties of as-cast c.p.Ti, binary Ti-40Nb and Ti-10Sn, and ternary Ti-10Nb-5Sn (at.%) to ascertain whether Sn content can be used as an enhancer for cell activity. From a metallurgy viewpoint, a range of binary and ternary alloys displaying distinctive Ti phases (i.e. β, α', α'') were achieved at room temperature. Their surface (oxide thickness and composition, roughness, contact angle) and bulk (compressive stiffness, strength, elongation, microhardness, electrical resistance) features were characterised. The same surface roughness was imparted on all the alloys, therefore substrate-cell interactions were evaluated independently from this variable. The physico-mechanical properties of the ternary alloy presented the highest strength to stiffness ratio and thereby proved the most suitable for load-bearing orthopaedic applications. From a cellular response viewpoint, their cytotoxicity, ability to adsorb proteins, to support cell growth and to promote proliferation were studied. Metabolic activity using a mouse model was monitored for a period of 12 days to elucidate the mechanism behind an enhanced proliferation rate observed in the Sn-containing alloys. It was hypothesised that the complex passivating surface oxide layer and the bulk inhomogeneity with two dominant Ti phases were responsible for this phenomenon.

Keywords

Titanium, Niobium, Tin, bulk properties, surface properties, pre-osteoblasts

1. Introduction

Titanium (Ti) and its alloys attract much interest due to their low density, manufacturability, corrosion resistance, non-toxicity, bio-inertness and highly tuneable bulk mechanical properties arising from different approaches to alloying and thermal post-processing routines. The use of alloying elements has permitted the modulation of a lower stiffness and a higher strength than pure Ti at room temperature. This is an attractive proposition when bone-mimicking properties are sought, because side effects such as stress shielding leading to

[1] Corresponding author; email: c.torres@lboro.ac.uk; phone: (+44) 1509 227 518

osteopenia and implant loosening are undesirable [1]. Ti, intended for bioengineering applications [2, 3], has been alloyed with elements such as Niobium (Nb), a beta stabiliser which suppresses the formation of equilibrium hexagonal closed-packed (hcp) α, martensite hcp α' and orthorhombic α'' when quenching to room temperature, and Tin (Sn), a low-cost neutral stabiliser that diminishes the formation of the embrittling isothermal ω phase, stabilising the β phase and therefore lowering the stiffness.

A visual representation of the prior work reported on Ti-Nb-Sn alloys is presented in Figure *1*. Caution has been exercised when selecting relevant studies due to the different manufacturing processes, thermal/mechanical post-treatments (e.g. rolling and ageing) available, as well as the range of methods used for measuring mechanical properties. For the purpose of this compilation, only arc-melting with water-chilled crucible casting and no further thermomechanical work, and quasi-static assessment of mechanical properties have been considered. Where experimental data was not available, *in silico* calculations using the Morinaga et al. '*Bo-Md diagram'* based on electronic theory has been used [4]. Four distinctive areas can be identified in Figure 1 that contain the different allotropic phases of Ti in different proportions: (1) α alloys, obtained with α stabilisers or neutral elements, such as Sn, and near α alloys, comprising <10 wt.% content of Nb, (orange and yellow regions in Figure *1*, including a non-quantified area of intermetallics for the Ti-Sn binary alloy); (2) α + α'' martensitic alloys: where the hcp-α/α' and the α'' orthorhombic phases co-exist in different ratios (yellow and green regions), (3) α'' + β alloys: with the further addition of Nb, and/or Sn, the parent β phase becomes apparent and both phases co-exist at different ratios (green-blue transition region); (4) metastable and stable β alloys (blue region): stable β alloys are reported when the Nb content surpasses 35 wt.% [5-7]. Considering Figure 1, the transversal cut from α/α', through α'' to β has been explored for the binary Ti-Nb [8-12] and Ti-Sn [13-17] alloys. Data from reported ternary Ti-Nb-Sn alloys [18-21] have been used for this compilation.

Journal Pre-proof

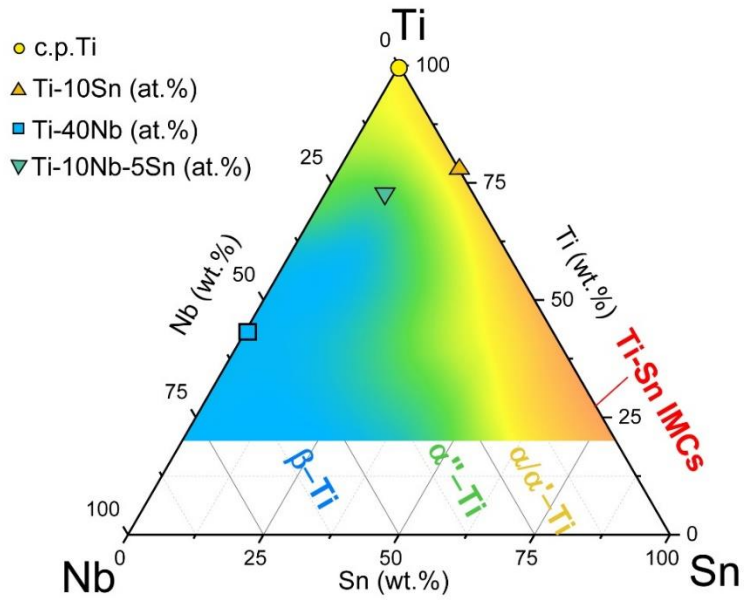

Figure 1: Visual representation depicting variations in phase content for the Ti-Nb-Sn alloys surveyed. The four alloys in this study are annotated with symbols

From the literature reported it is clear that Ti-Nb and Ti-Nb-Sn alloys, and specifically the metastable alloys due to their reported lower modulus of elasticity, have been studied extensively but this is not the case for Ti-Sn alloys despite Sn not being of a marked cytotoxicity, even in large amounts [22]. As well as bulk properties, surface features have also received much consideration since surface energy (correlated with hydrophilicity), net charge and roughness of metal oxides have all been identified as the most relevant properties that drive biological responses, in particular at the early stages of cell-surface interactions, from protein adsorption to subsequent osteoinduction towards finally bone mineralisation [23-25].

Although binary and ternary Ti-Nb-Sn alloys are strong contenders for tissue engineering, a systematic study on the Ti phases, bulk and surface properties has not been reported to the authors' knowledge, and inter-study comparisons are not possible due to disparities of manufacturing/characterisation methods employed. In particular, the impact of Sn addition has not been addressed despite the potential posed by this element to tune microstructure, modulate surface oxidation and therefore assess its impact on cell activity.

This is a hypothesis-driven study in which Ti-based alloys were designed using the *Bo-Md* electronic method to obtain exemplars of Ti phases (hcp, martensite and beta), manufactured and characterised with regards to their (i) bulk properties (physico-mechanical properties and electrical resistance) and (ii) surface features (suboxides, roughness and hydrophilicity to polar liquids), to assess their bioactivity behaviour and elucidate whether Sn

in their composition could enhance cellular metabolism during an *in vitro* study using an animal model (mouse pre-osteoblasts).

2. Experimental methods

2.1. Materials and processing

The alloys were created from powders (99.5% purity Ti, 99.8% purity Nb and 99.8% purity Sn powders, -325 mesh size, Alfa Aesar, UK) mixed at the corresponding ratios to achieve Ti-10Sn, Ti-40Nb and Ti-10Nb-5Sn alloy (at.%) and cold-isostatically compacted to 35 MPa to form green pellets. Pure Ti samples were also prepared for comparison purposes ('as-cast' c.p.Ti). To ensure a homogeneous composition at least five flips of the green pellet were carried out during arc melting (MAM-1 Edmund Bühler Compact Arc Melter, Germany) in a Zr-gettered Ar-atmosphere followed by suction casting in a water-cooled mould to obtain cylindrical ingots of approximately 10 mm diameter and 12 mm height and left to cool for at least 10 min, without any post processing.

2.2. Specimen preparation

For microscopic characterisation and microhardness testing the as-cast ingots were sectioned transversely (IsoMet 15HC blade with a Buehler IsoMet High Speed Pro, Germany), mounted in epoxy resin, ground with P400 grit SiC abrasive paper and polished with 9 µm diamond suspension and 0.02-0.06 µm colloidal silica. For surface morphological observations, 20 vol% H_2O_2 was added to the colloidal silica dispersion in the final step to reveal the microstructures. For surface characterisations (i.e. contact angle measurements and X-ray photoelectron spectroscopy (XPS)), the ingots were transversely sectioned into discs of 1.5 mm thickness and ground with P400 and P600 grit SiC paper. The grinding process was performed on all specimens until the same surface roughness was achieved without surface deformation. For the *in vitro* studies, the discs (1.5 mm thickness and 10 mm diameter) were cleaned as per the procedure reported in [26]. The samples were sterilised in an autoclave at 121 °C for 1 h and thoroughly rinsed in deionised sterile water.

2.3. Microstructure and surface characterisation methods

Back Scattered Electron (BSE) imaging, Secondary Electron imaging, Energy Dispersive X-ray (EDX) Spectroscopy and Electron Back Scattering Diffraction (EBSD) analyses were performed using a scanning electron microscope (SEM) (JEOL/ZEISS JSM 7800F FESEM, Japan). For EBSD, the step size was adjusted (from 0.05 to 4.2 µm) to the size of the observed features due to different scales present across the sample set. The X-ray diffraction (XRD) patterns were obtained on a Bruker D2 diffractometer, equipped with Cu Kα radiation (λ=0.15418 nm), 30 kV of voltage and 10 mA of current. X-ray Photoelectron

Spectroscopy (XPS) measurements were carried out on a spectrometer (K-alpha Thermo-Scientific, UK) with an Al source and spectra were curve-resolved (Avantage software with a Shirley-type background function) and charge-corrected to adventitious C 1s spectral component (C-C, C-H) at a binding energy of 284.8 eV. Ar ion monomer sputtering was utilised to acquire a depth profile of the oxide composition and chemistry, with a low ion energy of 500 eV (to minimise potential artificial chemical reduction of Ti and Nb oxide species) and raster size of 3 mm, yielding a sputter rate of 0.02 nm/s (reference to Ta_2O_5). Metrology measurements were carried out using an Infinite Focus microscope (Bruker Alicona, Germany) with TalyMap Platinum software (Taylor Hobson, UK) using 0.5 μm spacing resolution to obtain R_a (arithmetic mean deviation of the roughness profile) and R_{Sm} (mean width of the roughness profile) measurements. For contact angle measurement, the Sessile Drop method was carried out utilising an OCA-series contact angle system (Dataphysics Instruments, Germany). Two solutions, Minimum Essential Media (MEM) with added L-glutamine and Dulbecco's phosphate-buffered saline (PBS) solution were employed in tests conducted at ambient conditions recorded at 2 s after drop deposition. The same cleaning procedure for contact angle measurement was used [26]. Electrical resistance was assessed as sheet resistance using a 4-point probe fitted to a meter (2400 SourceMeter, Keithley Instruments Inc, USA) at ambient conditions.

2.4. Mechanical characterisation

Vickers microhardness test was performed at room temperature to assess the mechanical properties of the ingots, following the metallographic approach stated above (except the H_2O_2). The load applied was 9.807 N (HV1) with a holding time of 15 s. The microhardness mapping was conducted using a load of 0.4903 N (HV0.05) and a step size of at least four times the indent size.

Compression testing was conducted according to the ASTM E9 standard on samples machined from the ingots using a lathe to achieve a cylinder of 6 mm diameter and 12 mm height (i.e. L/D = 2). Top and bottom faces were ground with P800 grit SiC paper to remove residual rims, burrs and avoid friction against the UTM platens (T489-73/74) on a 3369 frame fitted with a 50 kN load cell (2530-445) and a LVDT deflection sensor (2601-062) (Instron, UK). A monotonic load at a constant strain rate ($4.58e^{-5}$ s^{-1}) was applied until plastic deformation was observed. A compliance correction was included in the calculations. The compressive stiffness, i.e. the Young's Modulus, was calculated from the gradient formed between stress-strain and the yield strength was calculated from the departure of linearity in the elastic region.

2.5. *In vitro* testing and biocompatibility assessment

Journal Pre-proof

2.5.1. Cell line and culture media preparation

Culture media was prepared using essential α-MEM enriched with 10% fetal bovine serum FBS (Thermo Fisher Scientific, UK), 1% L-glutamine, and 1% Penicillin-streptomycin (Sigma, UK). Mice pre-osteoblast line MC3T3-E1 at passage 9 were incubated in a 5% CO_2 atmosphere at 37 °C (Thermo Scientific Heracell™ 150, UK). Upon 80% confluency, cells were detached using Trypsin EDTA (0.25% w/v trypsin/0.02% EDTA) (Gibco, Thermo Fisher UK) centrifuged at 150*g for 5 min and seeded onto the pre-conditioned (i.e. soaked in cell culture media overnight) discs placed in a 24-well low adhesion plate. Media was changed every 2 days for the entire duration of the experiment.

2.5.2. Cytotoxicity, cell expansion and DNA content quantification

Cell response to the alloys was studied using a negative/positive control approach. Pure Aluminium (Al) and Copper (Cu), known for their high cytotoxicity [27], discs of same dimensions to the Ti alloys discs (10 mm diameter, 1.5 mm height, Smiths Metal Ltd, UK) were used as negative controls. The polystyrene (PS) of the well plates was used as a positive control. 50,000 cells were seeded on each disc and their behaviour monitored for 48 h using an optical microscope (EVOS XL, Invitrogen, UK). A combination of fluorescent dyes diluted in Hexamethyldisilazane (HBSS) solution (Sigma Aldrich, UK) (i.e. 10 µM CMFDA (5-chloromethtlfluorescein diacetate, Thermo Fisher Scientific, UK), designed to freely pass through cell-walls where it is transformed into cell membrane-impermeant, was used to image alive cells; and 2 µg/ml Propidium Iodide (PI, Thermo Fisher Scientific, UK), a fluorescent nucleic acid intercalator agent which is not permeant to alive cells, used to stain dead cells) was added to the cell culture, previously rinsed in PBS (Sigma-Aldrich, UK), and incubated at 37°C. After 30 min the excess dye was removed with PBS, the cell culture medium replaced and cells visualized under the fluorescence microscope (Ex 492, Em 517) (Nikon Ti Eclipse, Japan).

Toluidine blue, a basic thiazine metachromatic dye with high affinity for acid tissue components, was used to qualitatively stain viable cells and monitor cell expansion 2 and 12 days after seeding. Using 4% Glutaraldehyde and after overnight refrigeration, the discs were washed with PBS, soaked with 0.01% w/v of Toluidine Blue in PBS and stored for 20 min at room temperature. Samples were then gently washed to remove any excess of Toluidine solution and purple-spotted surfaces photographed (Bruker Alicona, Germany).

DNA content on the discs was quantified using Pico Green® DNA kit (Quanti-iT Picogreen dsDNA, Invitrogen, UK). Samples were washed three times in PBS in order to remove any debris which could interfere with the fluorescent assays. Then, 500 µl of 0.1% Triton-X in

deionized water was added to each well and the plate was stored at -80 °C. In order to achieve complete lysis, the discs were cyclically frozen and thawed at room temperature three times. The cell lysate was collected and stored in 1.5 ml DNAse-free Eppendorfs. 25 µl of each cell/lysis buffer solution was placed into a 96 well plate with 75 µl of dH_2O to a 1:3 dilution. The Pico Green® solution was prepared as a 1:1,200 dilution in 1x Tris-EDTA buffer and 100 µl were added to each sample well. This was stored in darkness for 5 min before fluorescence readings were taken (Ex 480, Em 520 nm).

2.5.3. Protein adsorption

Six discs of each alloy were placed in a 24-well plate, soaked with 600 µl of 0.1% Bovine Serum Albumin BSA (Sigma Aldrich, UK) diluted in PBS and incubated in the protein solution. After 1 and 24 hours at 37 °C the specimens were washed with PBS in order to remove loosely attached proteins. The discs were thoroughly shaken in an orbital shaker (Sciquip, UK) and washed in 300 µl of PBS. The total number of proteins attached on the discs were quantified with 660 nm-Pierce Protein assay (Sigma Aldrich, UK). 10 µl of each protein solution were transferred into a 96-well microplate and 150 µl of reagent added to each well. The absorbance was measured at 600 nm using a microplate absorbance reader (Fluostar Omega, BMG Labtech, UK).

2.5.4. Cell metabolic activity

The discs capability to sustain proliferation was evaluated over 12 days. A 50 µl drop of culture medium containing 12,000 cells was seeded on each disc. After 2 h of incubation at 37 °C, cells adhered onto the material and 1.2 ml of cell culture medium was added to each well. Every second day 1ml of culture medium was collected and replaced with fresh medium. Media from the samples were stored at -20 °C prior to the measurement of Glucose concentration, its conversion to Lactate, and Lactate Dehydrogenase (LDH), an intracellular enzyme released into the media from damaged cells and marker of membrane integrity (Cedex Bio HT Analyzer, Roche, UK).

2.5.5. Cell morphology observation

On day 12 the discs were fixed with 4% glutaraldehyde in 0.1 M cacodylate buffer and refrigerated overnight. Treatment with 2% Osmium Tetroxide (OsO_4) for 2 h at room temperature followed by dehydration (15 min rinsing stages in increasing Ethanol concentration solution (30%, 50%, 70%, 95% and 100% in triplicate) and subsequent soaking in three HMDS solutions (2:1 pure ethanol in HMDS, 1:2 pure ethanol in HMDS and final 100% HDMS solution) and left to dry overnight. The discs were mounted and gold/palladium coat-sputtered for cell morphology analysis in SEM.

2.6. Statistical analysis

Statistical analysis for the electrical resistance and mechanical tests was performed using averages and standard deviation over the results obtained using the repeat specimens or the multiple tests over the same specimen, observing accuracy levels of the machine. Resistance tests were performed on five different spots, contact angle was performed on four samples per alloy and on at least five locations per disc, mechanical tests were performed in triplicate. Statistical analysis for the biological tests was performed using the computing environment R (R Development Core Team, 2005). Distribution of data was verified using the Shapiro Normality Test. Analysis of Variance was performed using the Bartlett test of homogeneity of variances and any significant differences in protein adsorption were detected using the Kruskal Wallis non-parametric test. Statistical analyses for metabolic studies were done using one-way ANOVA, T-test and Tukey post-hoc tests, and $p < 0.05$ were considered statistically significant.

3. Results

3.1. Microstructure and phase characterisation

Figure 2 depicts representative grain and phase characteristics of the as-cast c.p.Ti, Ti-40Nb, Ti-10Sn and Ti-10Nb-5Sn samples, observed on their transverse cross-section from SEM and EBSD analyses. The c.p.Ti displayed a basket-weave microstructure consisting of colonies of hcp-α' lamellae with a width of approx. 2-3 μm and in-plane size of ≥ 100 μm (Figure 2a-c, EBSD-indexed using hcp-α ($P6_3/mmc$)). The transverse cross section of the binary Ti-40Nb alloy (Figure 2d-f) presented a predominant β microstructure phase (EBSD-indexed through bcc-β (Im3m)) retained at room temperature. The ingot's centre displayed columnar β grain morphology, with a grain size spanning hundreds of micrometres and elongated towards the edge caused by a temperature gradient (Figure 2e-f). At the ingot edge, near the casting mould where rapid cooling occurs inducing constitutional supercooling, dendritic solidification with varying dendrite arms spaced at approximately 10 μm were observed (supplementary S1). As presented in Figure 2g-h, the binary Ti-10Sn alloy presented a *Widmanstätten* microstructure, consisting of colonies of largely parallel α' lamellae. Upon growth of the α' lamellae, Ti_3Sn intermetallic compound (IMC) particles, with an average size of tens of nm, were found to precipitate largely delineating the α' lamella boundaries and forming acicular inter-lamella platelets. The EBSD IPF map (Figure 2i) indicates that both Ti_3Sn and α' features were indexable using hcp-α ($P6_3/mmc$). Figure 2j-l shows that the ternary Ti-10Nb-5Sn ingot displayed a duplex-phase microstructure, consisting of equiaxed bcc-β grains of Ti (Nb, Sn) solid solution with a grain size of up to 1 mm and continuous colonies of acicular, orthorhombic α'' nano-needles (ca. 1 μm in length;

up to 250 nm in width) distributed through the β grain boundaries. Small sizes and high density of lattice defects of the α'' features presented difficulties in indexation (white areas in Figure 2l).

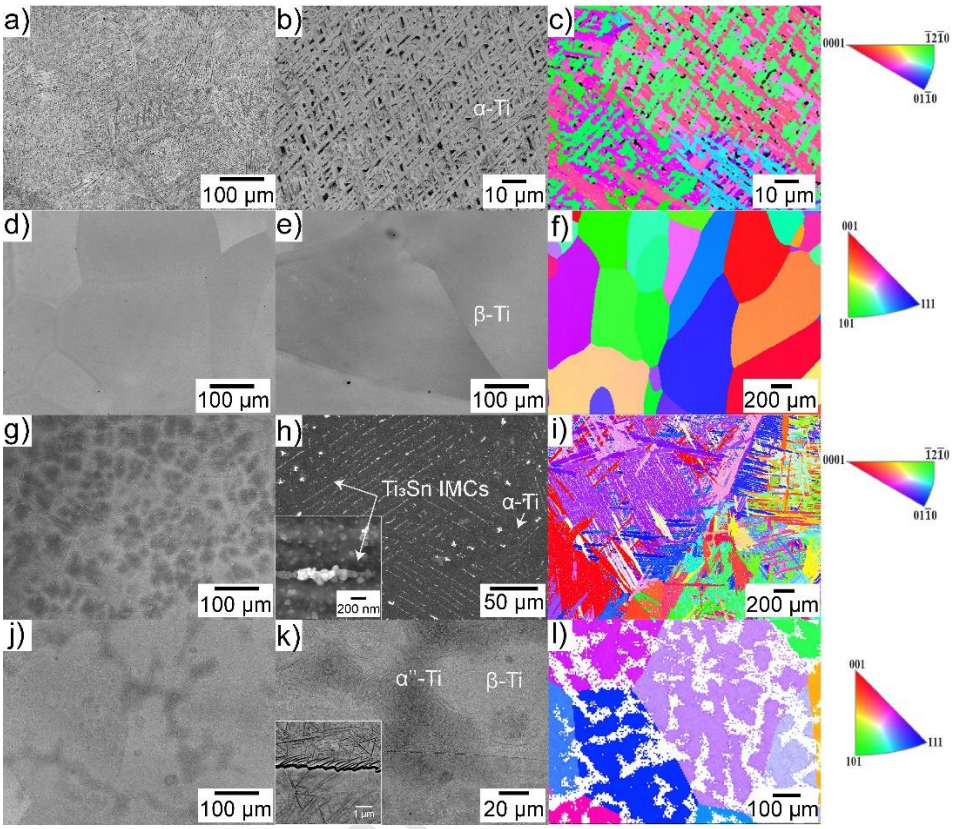

Figure 2: Representative backscattered electron (BSE) images and EBSD IPF-Z maps for: (a-c) c.p. Ti, (d-f) Ti-40Nb, (g-i) Ti-10Sn, inset in (h) magnification into IMCs, (j-l) Ti-10Nb-5Sn, inset in (k) magnification of acicular α'' features. Standard stereographic triangles show a colour-coded schematic grain orientation dependence on different planes

Figure 3 shows the XRD results from the alloys under study. The phase characteristics of the c.p.Ti (Figure 3a) shows a predominant single hcp phase without any evident preferred grain orientation. Because the lattice constant of the hcp α' and the hcp α cannot be discriminated only by XRD, we have labelled those peaks α/α' in Figure 3. A predominant β phase was confirmed for Ti-40Nb (Figure 3b) alongside marginal orthorhombic α'' reflections. The hcp-α'(or α) reflections in Ti-10Sn (Figure 3c) substantiate the results from EBSD. The duplex-phase observed on the Ti-10Nb-5Sn was confirmed with XRD analysis (Figure 3d).

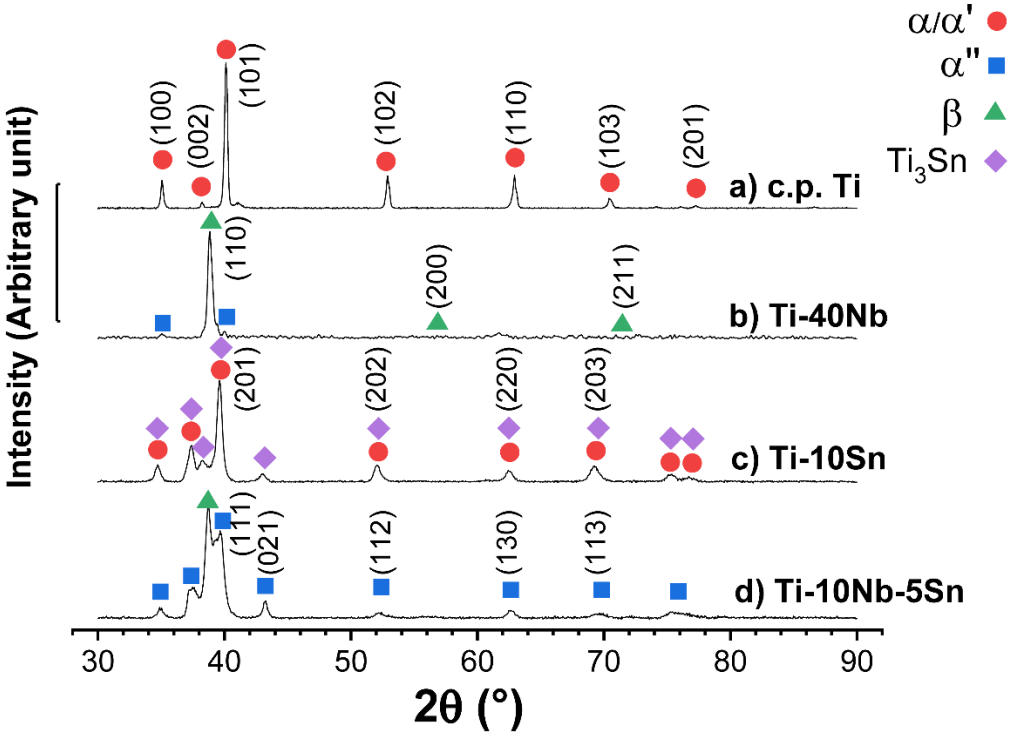

Figure 3: X-ray diffraction patterns of as-cast c.p.Ti and Ti-based alloy specimens

3.2. Surface characterisation: oxidation, roughness and contact angle

Figure 4 presents the results from surface oxide analysis using XPS. The deconvoluted peaks analysed were Ti2p, Nb3d and Sn3d. Three chemical states of Ti species were identified (in the primary XPS region $Ti2p_{3/2}$): TiO_2 at binding energies 458.0-458.2 eV, Ti_2O_3 at 456.0-456.3 eV and Ti^0 metal at 453.0-453.2 eV. Three chemical states of Nb species were observed from the two Nb-containing compositions (referred to $Nb3d_{5/2}$): for Ti-40Nb, Nb_2O_5 at binding energy 206.9 eV, Nb_2O_3 at 204.2 eV and Nb^0 metal at 201.6 eV; whilst for Ti-10Nb-5Sn, Nb_2O_5 at 206.7 eV, Nb_2O_3 at 203.5 eV and Nb^0 metal at 201.6 eV. In addition, two chemical states of Sn species were observed from the two Sn-containing compositions (referred to as $Sn3d_{5/2}$): for Ti-10Sn, SnO_x at binding energy 485.7 eV and Sn metal at 483.4 eV; whilst for Ti-10Nb-5Sn, SnO_x at 486.0 eV and Sn metal at 483.8 eV.

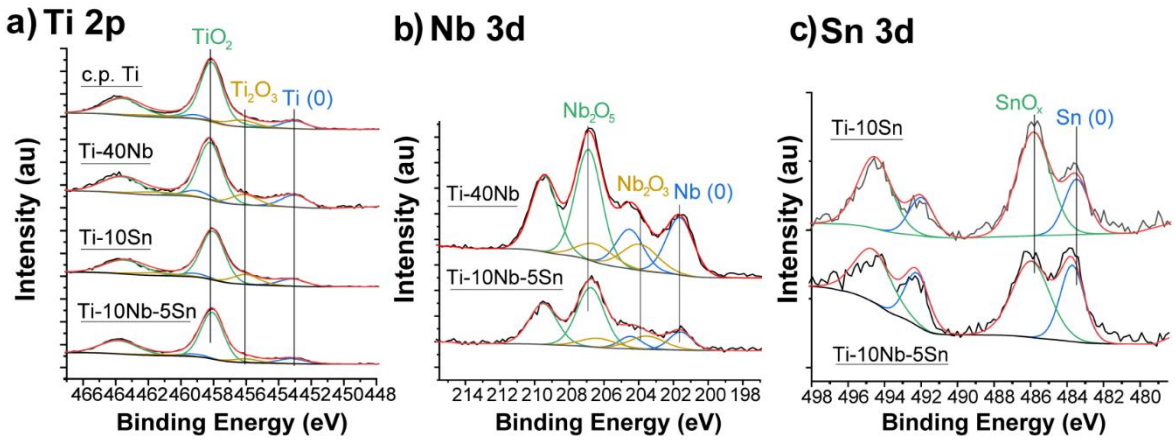

Figure 4: Deconvoluted XPS narrow spectra of a) Ti2p, b) Nb3d and c) Sn3d collected from the specimen surface of the four compositions without any ion sputtering

The in-depth chemical and compositional distribution profile of the oxide layers (Figure 5) are reported in Table 1. The oxide thickness was estimated where the oxygen content diminishes to half of its highest value. The oxidation of Ti in air gave predominantly TiO_2 and marginally Ti_2O_3. Ti-40Nb presented 53.5 at.% titanium oxides (TiO_2 +Ti_2O_3, the former being predominant) and 46.5 at.% niobium oxides (Nb_2O_5 +Nb_2O_3, the former being predominant). Ti-10Sn presented 92.8 at.% titanium oxides (TiO_2 +Ti_2O_3, the former being predominant), the remaining 7.3 at.% being a tin oxide. Ti-10Nb-5Sn exhibited 81 at.% titanium oxides (predominantly TiO_2), 16.5 at.% niobium oxides (predominantly Nb_2O_5) and 2.5 at.% SnO..

Journal Pre-proof

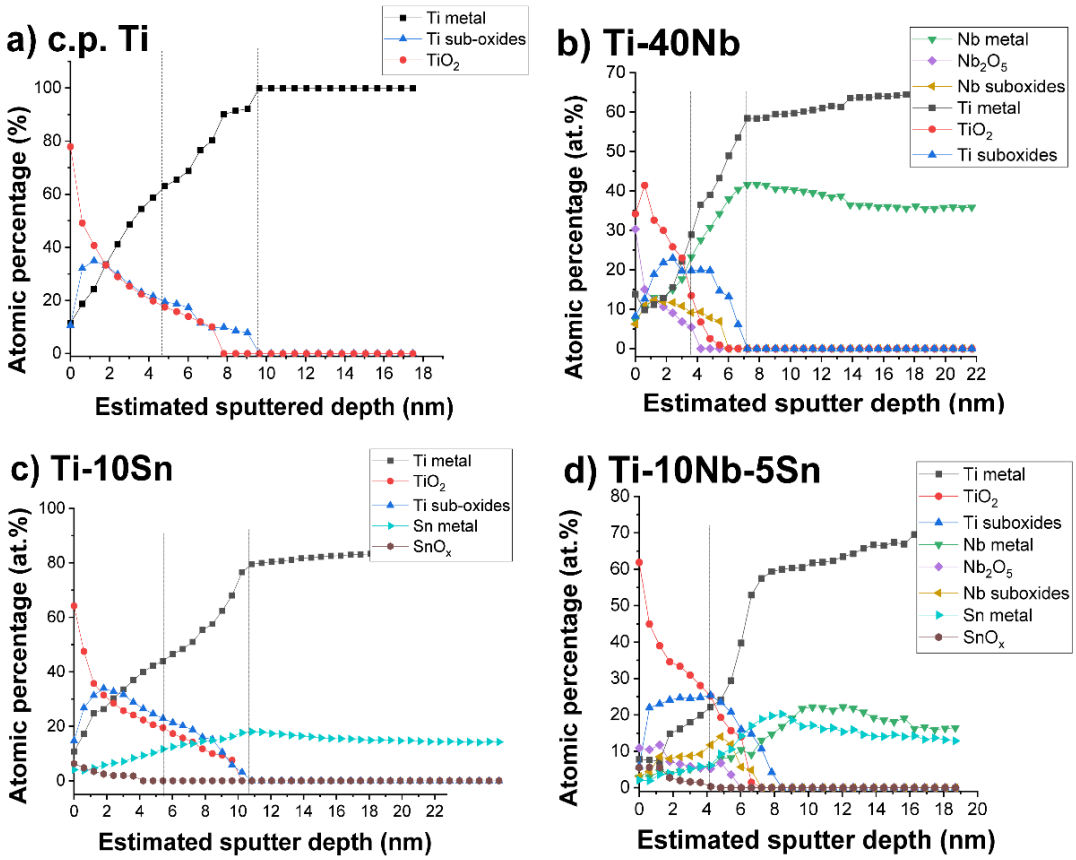

Figure 5: XPS compositional and chemical depth profiling acquired from the surfaces of as-cast a) c.p. Ti, b) Ti-40Nb, c) Ti-10Sn and d) Ti-10Nb-5Sn

Table 1 also summarises the results obtained from the surface measurements including the roughness profile and the contact angles on each of the samples as per the sessile drop method with two solutions (PBS and MEM + L-glutamine), media used in the *in vitro* studies.

Table 1: Surface features: oxidation (XPS-derived oxides inventory), roughness and contact angle (on MEM-Lglutamine and PBS) measurements.

Sample ID	Oxide in surface, at.%†						Roughness		Contact angle	
	Oxide thickness, nm§	TiO_2	Ti_2O_3	Nb_2O_5	Nb_2O_3	SnO_x	R_a, um	R_{Sm}, um	MEM+Lglut, °	PBS, °
c.p.Ti	~ 4.8	88.4	11.6	-	-	-	0.367 ±0.008	21.186 ±5.714	40 ± 3	49 ± 2
Ti40Nb	~ 3.6	45.0	8.5	35.3	11.2	-	0.352 ±0.165	18.627 ±3.882	46 ± 2	58 ± 2
Ti10Sn	~ 5.4	76.0	16.8	-	-	7.2	0.334 ±0.0308	19.599 ±2.765	57 ± 3	67 ± 1
Ti10Nb5Sn	~ 4.1	74.0	7.0	12.9	3.7	2.5	0.4246 ±0.185	28.019 ±4.581	32 ± 3	48 ± 2

§ The oxide thickness was estimated where the oxygen content diminishes to half of its highest value (indicated by dashed lines in Figure 5)
† Sampling depth 3-5 nm

Table 2 presents the results from the physico-mechanical tests on the bulk specimens. The electrical sheet resistance results are listed in this group as it is most probable that the 4-point probe penetrated through the nanometric native oxide layer on the specimen surface, indicated by the large SD values of the measurements, in particular those of the c.p.Ti and Ti-10Nb-5Sn. Although the electrical sheet resistance is a property independent of the oxide layer thickness, it can be argued that these values probably represent the bulk electrical characteristics and are not exclusive to the surface oxide.

Table 2: Bulk properties: Metallurgy: Titanium allotropic phases present in each alloy; Electrical (sheet) resistance; Mechanical properties: Vickers microhardness, compressive stiffness, yield strength and strain at yield

Sample ID	Phase	Electrical resistance, Ohm/sq	Microhardness (HV1), GPa (±SD)	Young's Modulus, GPa	Strength at yield, MPa	Strain at yield, %
c.p.Ti	α /α'	$1.87e^{-2}$ ± $4.9e^{-3}$	3.27 ± 0.22	99.99 ± 2.44	846.61 ± 34.40	0.99 ± 0.08
Ti40Nb	β (minor α'')	$9.75e^{-3}$ ± $3.2e^{-3}$	3.44 ± 0.07	80.75 ± 1.77	994.37 ± 40.01	1.36 ± 0.05
Ti10Sn	α' + Ti_3Sn IMCs	$9.37e^{-3}$ ± $2.4e^{-3}$	3.96 ± 0.15	78.68 ± 2.12	922.64 ± 37.79	1.33 ± 0.06
Ti10Nb5Sn	β + α''	$1.21e^{-2}$ ± $4.4e^{-3}$	3.83 ± 0.41	65.19 ± 1.97	1283.38 ± 52.31	2.19 ± 0.09

The microhardness value for the ternary Ti-10Nb-5Sn alloy presented a large standard deviation value. This can be explained by the variation in microhardness values (Figure 6) when an exhaustive mapping on the alloy was performed.

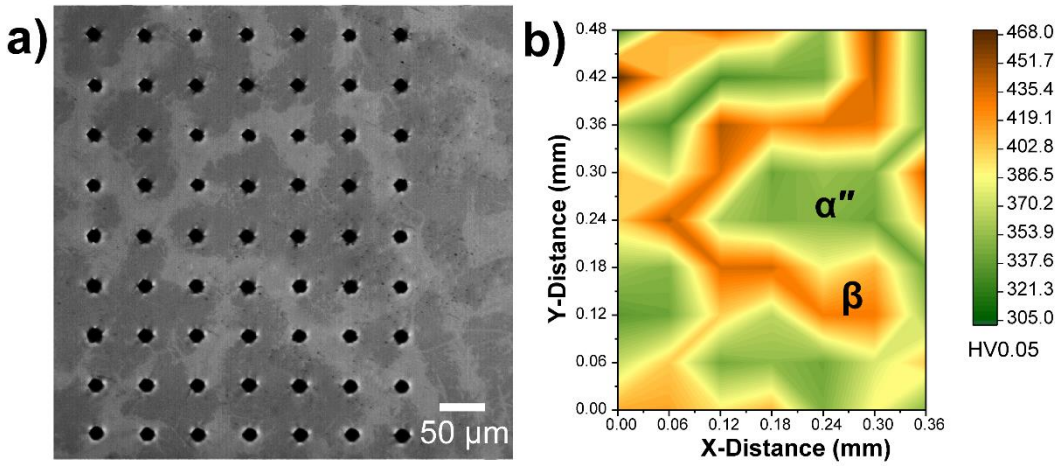

Figure 6: Microhardness mapping on the Ti-10Nb-5Sn alloy depicting local variations of HV0.05 value depending on Ti phase

3.3. Biological *in vitro* results

3.3.1. Cytotoxicity

Cells were co-cultured with the Ti-based alloys and negative controls (Al and Cu) for 24 and 48 h. Figure 7a shows the extent of cell survival in the cultures incubated with the alloys (after 24 h: 95.96 ± 1.16%, after 48 h: 93.92 ± 1.15%) and the extent of cell death (100%) in the cultures with the negative controls. The morphology of the cells incubated with the alloys was extended and filamentous as observed in the fluorescence (Figure 7b-e) and microscope images (Figure 7h-k). What remained of the cells incubated with the negative controls was debris from the ruptured membranes (Figure 7f-g, l-m).

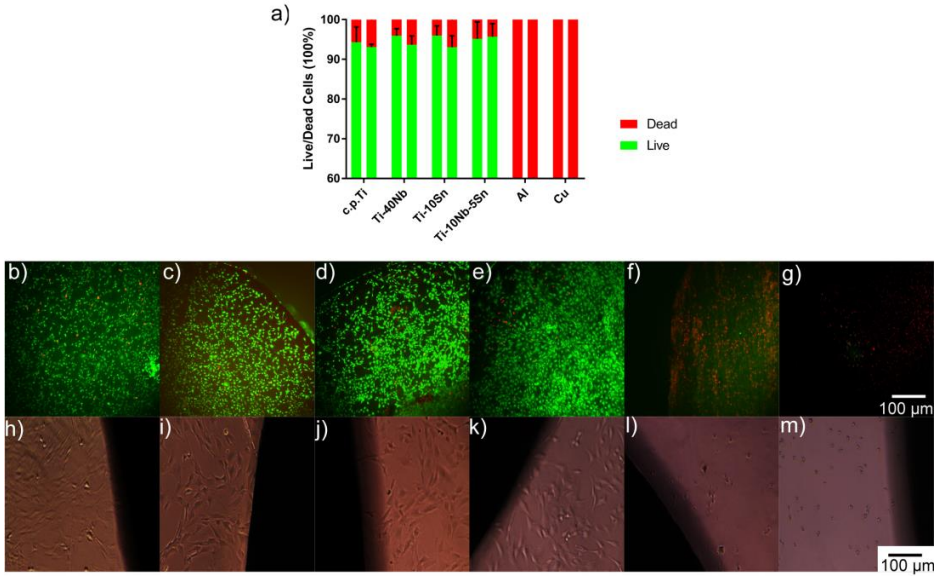

Figure 7: (a) Live/Dead assay results for MC3T3-E1 cells co-cultured for 24 h (first column) and 48 h (second column) with (b,h) c.p. Ti, (c,i) Ti-40Nb, (d,j) Ti-10Sn, (e,k) Ti-10Nb-5Sn alloys and (f,l) Aluminium, (g,m) Copper metals

3.3.2. Cell proliferation and morphology

Toluidine blue evaluated qualitatively cell growth and expansion on the discs. Blue spots indicated the presence of metabolic-reactive cells on the alloys surfaces after 2 (Figure 8a-d) and 12 days of incubation (Figure 8e-h), displaying full confluence. Colonisation on the surfaces of all the specimens was extensive and dense and the cells demonstrated healthy proliferation, with filamentous morphology as per SEM observation of their cytoskeletons (Figure 8i-l). DNA was quantified and further confirmed that the cell density at day 12 on all discs was equal and the cell colonies confluent, (reported as DNA content and normalised by the surface area, c.p.Ti 226.389 ± SD 33.371, Ti-40Nb 226.683 ± 17.521, Ti-10Sn 209.107 ± 22.303, Ti-10Nb-5Sn 209.492 ± 20.148 ng/cm^2, indicative of cell numbers).

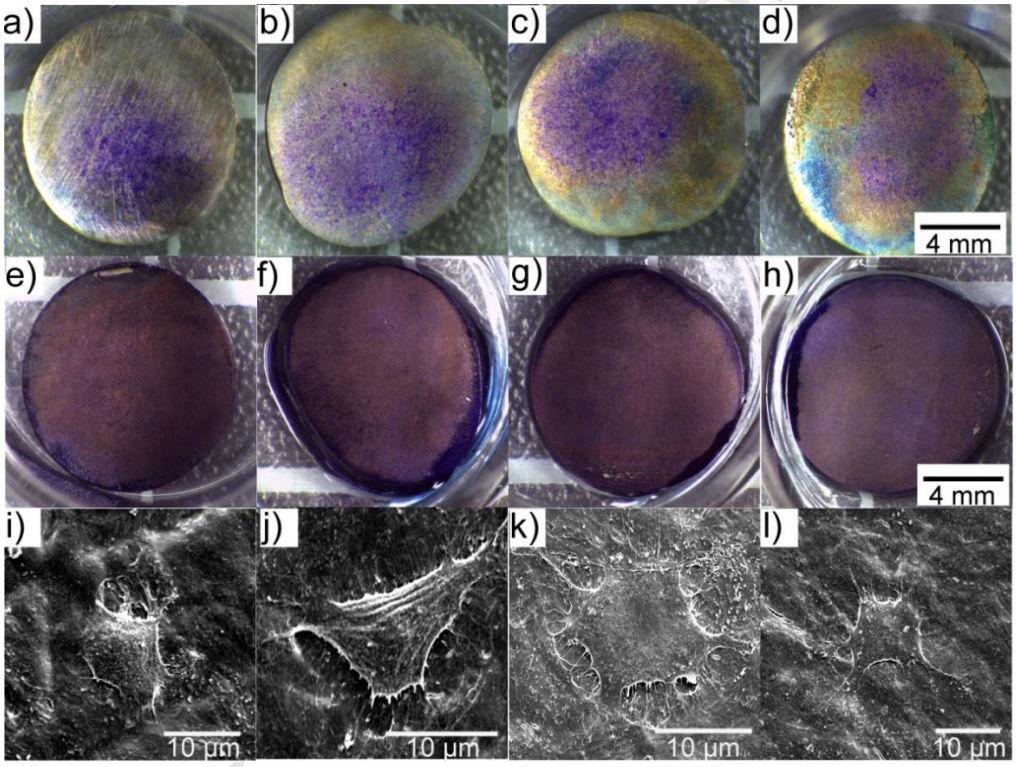

Figure 8: Qualitative cell expansion: at (a-d) day 2 and (e-h) day 12 evaluated with Toluidine Blue staining and (i-l) SEM imaging of cells at day 12 on (a,e,i) c.p.Ti, (b,f,j) Ti-40Nb, (c,g,k) Ti-10Sn, (d,h,l) Ti-10Nb-5Sn alloys

3.3.3. Protein adsorption tests

Figure 9 presents the results from protein adsorption, by measurement of albumin adsorption, tests after 1 h and 24 h.

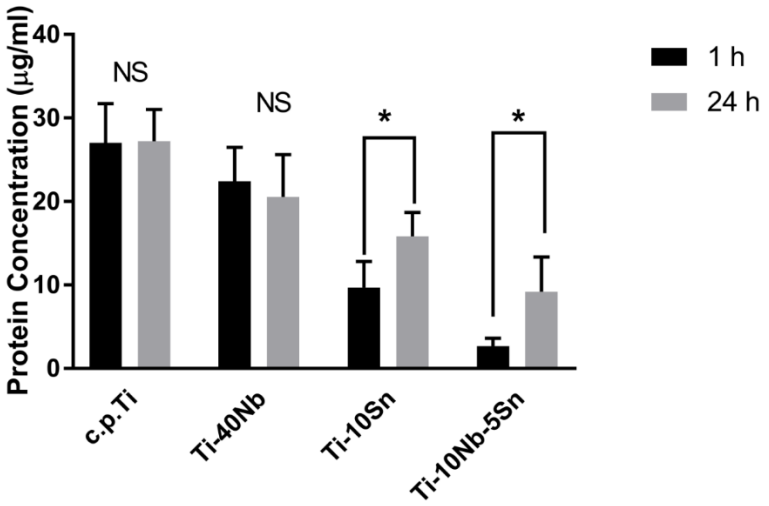

Figure 9: Concentration of albumin absorbed on discs surfaces after 1 and 24 h (* denotes value $p<0.05$)

3.3.4. Effect of the alloys on cell metabolic activity

Quantification of metabolites over a period of 12 days confirmed that cells proliferated throughout the duration of the study. Figure 10 shows the glucose consumption as well as the lactate production rates. No detectable quantities of LDH were observed (below the sensitivity threshold of detection <20 U/ml) over the duration of the experiment and therefore are reported as nil. Levels of glucose and lactate normalized by the DNA concentration were further compared and analysed at day 12 of the experiment (Figure 11), when cells colonised the surface of the implant as informed by the proliferation study (Figure 8e-h).

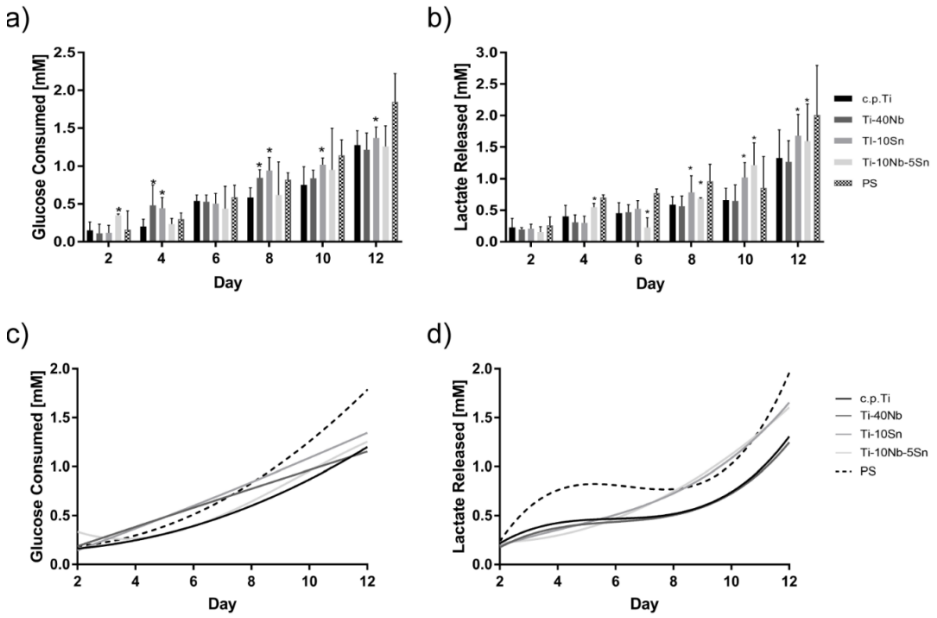

Figure 10: Metabolic activity measured as (a,c) glucose consumption and (b,d) lactate released during 12 days by the MC3T3-E1 cell culture on the c.p.Ti, Ti-40Nb, Ti-10Sn, Ti-

10Nb-5Sn and the well material used as a positive control (* denotes p<0.05 compared to c.p.Ti)

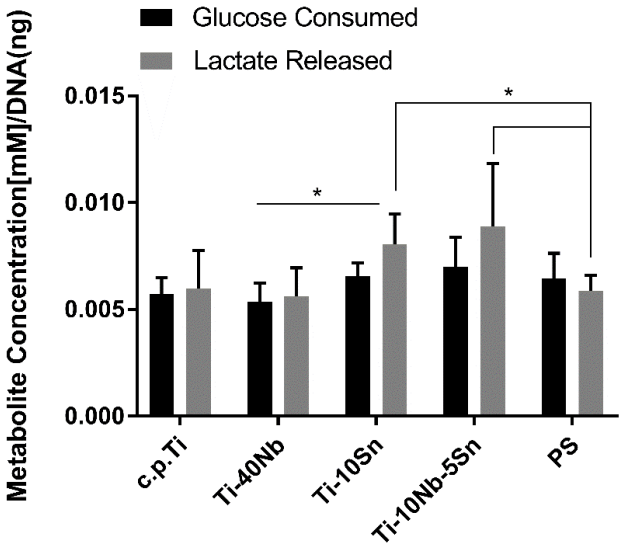

Figure 11: Metabolic activity (glucose consumption and lactate release) at day 12 normalized by the number of cells (* denotes p<0.06 compared to c.p.Ti)

4. Discussion

4.1. Phase metallurgy and microstructure

The c.p.Ti basket-wave microstructure was due to large cooling rates at casting. The nucleation and growth of hcp-α' initiated from prior β grain boundaries where colonies of parallel hcp lamellae emerged, followed by lamellar growth in a near-perpendicular direction to the existing α lamellae. The metastable Ti-40Nb presented, as expected and in agreement with literature, large β grains. The *Widmanstätten* microstructure of Ti-10Sn (i.e. duplex-phase colony microstructure consisting of hcp-α lamellae and inter-lamellar hexagonal Ti_3Sn IMC nanoplatelets) was similar to that found in Ti-18Sn (wt.%) [15]. The Ti-10Sn ingots exhibited certain compositional fluctuations, not only due to formation of Ti_3Sn IMCs (enriched in Sn to 25 at.%) (as shown in supplementary S2) within hcp-α' colonies, but also owing to segregation of Sn across α colonies presumably into regions between α dendritic arms, evidencing itself as a brighter contrast from BSE imaging (Figure 2g). The orthorhombic α'' nano-needles distributed through the β grain boundaries in Ti-10Nb-5Sn appeared in triangular configuration generated as a result of the recrystallisation of the material, and has also been observed elsewhere [28]. In terms of composition, the α'' phase was enriched in Sn and depleted in Nb, as seen in elemental maps shown in supplementary S3. These point to the likelihood that the solidification proceeded first with the formation of β dendrites collecting β-stabilising Nb solutes and ejecting Sn solutes into the adjacent inter-

dendritic liquid, followed by solidification of the remaining liquid region precipitating α'' due to a local depletion of the β stabiliser and delineating the region in between β dendritic arms.

4.2. Oxide(s) layer: XPS native oxide analysis

Figure 4 depicts deconvoluted XPS narrow spectra of Ti2p, Nb3d and Sn3d from c.p.Ti, Ti-40Nb, Ti-10Sn and Ti-10Nb-5Sn alloys surfaces. For the Ti2p species no significant energy binding shifts were observed in Ti-40Nb compared to c.p.Ti, probably due to the similar electronegativity values of Ti and Nb (1.54 and 1.60, respectively). Ti-10Sn and Ti-10Nb-5Sn displayed an approx. 0.2 eV shifts towards lower binding energies, attributable to electronegativity dissimilarity between Ti and Sn (1.54 and 1.96, respectively) [29]. The energy binding values of the Nb3d species were about 0.5-0.7 eV lower than those normally observed [30] using similar XPS analysis conditions, which suggests the possibility of substitution of Ti by Nb in the oxides. The oxide species of Sn (Sn3d) were assigned as SnO_x ($1<x<2$), due to similar binding energies of SnO and SnO_2 and also to possible spontaneous conversion from SnO to SnO_2 [31], both compromising an exact chemical state determination of Sn oxides. It is worth noting that the binding energy values of Sn metal component for both the compositions were about 1.4-1.8 eV lower than those observed from pure Sn metal [32]. Such shifts may also be ascribed to the electronegativity dissimilarity between Sn and Ti (Nb).

Table 1 and Figure 5 present the XPS-derived atomic percentages of various components accounting for the air-formed oxide layers of the c.p.Ti, Ti-40Nb, Ti-10Sn and Ti-10Nb-5Sn. The Ti-40Nb presented an amount of titanium oxides larger than niobium oxides, suggesting a competing oxidation process that resulted in Ti-Nb-O oxides. In contrast, results from Ti-10Sn and Ti-10Nb-5Sn show that the Sn oxidation was less competitive. These results suggest that the oxidation tendency of co-existing Ti, Nb and Sn elements follows the order: Nb > Ti > Sn. This tendency is consistent with the Standard Gibbs free energy change ($-\Delta G_f^{\circ}$) trend and is indicative of spontaneous oxidation at T_{room} 293 K: Nb_2O_5 (1766 kJ/mol) > TiO_2 (891.2 kJ/mol) > SnO (254 kJ/mol) [33].

4.3. Roughness and contact angle measurement

The same surface finish protocol was applied to all the specimens to achieve similar surface roughness values on all samples (Table 2). This allowed a direct comparison of hydrophilicity derived from the chemistry of the surfaces, independent from any physical attribute derived from its surface roughness. This target value was informed by similar R_a values used successfully in other studies with titanium alloys with the same cell lineage [34] and other osteoblasts [35]. In all cases, regardless of the liquid media used, the surfaces

were wetted (i.e. angle <90°). The culture media component (MEM/L-glutamine) displayed smaller contact angles than those when the protein-carrying PBS fluid was used, with c.p.Ti and Ti-10Nb-5Sn being particularly wettable. The contact angles using both the MEM/L-glutamine and PBS fluids were, in ascending order, Ti-10Nb-5Sn < c.p.Ti < Ti-40Nb < Ti-10Sn, and these were negatively correlated to the small variations in surface roughness features (R_a, R_{Sm}).

4.4. Mechanical properties: Vickers Microhardness and compression testing

The single-phase hcp-α/α' c.p.Ti exhibited an average hardness of 3.27 GPa and the (mainly) single phase β-based Ti-40Nb displayed 3.44 GPa as hardness. Solid solution strengthening from Nb into Ti is suspected to be responsible for this increment, as reported elsewhere [36]. The hardness of α'-phase Ti-10Sn was 3.96 GPa, considerably higher compared to the former two, which could be attributed to the precipitation hardening arising from the widespread presence of inter-α-lamellar Ti_3Sn IMCs in Ti-10Sn (Figure 2h) as well as solid solution strengthening with Sn content [14]. The duplex-phase (β + α'') Ti-10Nb-5Sn alloy displayed higher values of hardness (when measured using HV1 (9.807 N)) than the single phase β-based alloy. An increment in hardness for the duplex (β + α'') versus the single β alloy has also been reported in Ti-Nb binary systems [8] as well as in Ti-Nb-Sn ternary alloys [39]. We hypothesise that this is due to a β - α'' strain-induced transformation, providing a hardening effect overall, as observed in [38], because α'' is harder than β [37]. Large variations in the microhardness values measured on the ternary alloy, ranging from 3.52 to 4.24 GPa (ave. 3.83 GPa), were due to the phase-dependence of the hardness, as shown in the hardness mapping (HV0.05 (0.4903 N)) (Figure 6). At this scale and payload, the β phase appeared to possess higher hardness values compared to that of α''. Larger values of microhardness in single β phase Ti-Nb-Mo-Sn alloys with respect to α'' phase have been reported [37] and have been attributed to solid solution hardening effects of Nb in this alloy.

The compression testing results yielded a range of Young's moduli from 99.99 to 65.19 GPa with the corresponding descending order: c.p.Ti > Ti-40Nb > Ti-10Sn > Ti-10Nb-5Sn. As expected, the stiffness value for c.p.Ti was the highest of the set and in agreement with literature [13, 18], where α' is reported as the stiffer phase of titanium. Ti-40Nb is a (mainly) single beta-phase (β) alloy and therefore its stiffness value is lower than that of c.p.Ti, in agreement with other reports [8, 18, 19]. Fully stabilised β-Ti alloys have been reported to display the lowest values of stiffness due to their body-centred cubic lattices but in this case this effect appears to be overridden by the solid solution strengthening of Nb (>50 wt.%) present in the alloy. This result matches those obtained from other heavily stabilised Ti-Nb alloys (Ti40Nb wt.%, 81 GPa [10]). Although the presence of intermetallics in Ti-10Sn (i.e. α'

precipitates embedded in an α' matrix to realise a coherent superstructure [40]) were expected to increase bulk stiffness, this mechanism did not realise and instead a bearing-like slip-rolling effect of the IMCs along the Ti-Sn grains decreased the overall stiffness value. A similar result of stiffness has been reported in Ti-Sn alloys with IMCs (Ti20Sn at.%, 75 GPa [16]). Finally, duplex-phase Ti-10Nb-5Sn possessed the lowest modulus of elasticity of the set compared to single phase α', α'' and stabilised β alloys. This drop in stiffness was expected due to three mechanisms: 1) Other reports of similar Nb/Sn balance [18, 19] have reported that the addition of Sn prevented the precipitation of ω phase and consequently the increase in stiffness; 2) The addition of Sn has also been reported to reduce modulus of elasticity in Ti-Nb alloys through extension of lattice parameters [41]; and 3) the presence of α'' phase increases internal friction deriving into weaker plastic deformation than when α' phase is present instead [42]. It is noteworthy that the ternary alloy displayed the largest elongation value (measured as strain at yield and reported as a % in Table 2), as expected from alloys containing thermally-induced α'' phase.

The yield strengths recorded for the alloys follow the reverse trend to that of the stiffness, being Ti-10Nb-5Sn the strongest alloy and c.p.Ti the weakest. Similar values for c.p.Ti have been reported in literature [13, 18]. To the best of our efforts, it has not been possible to find values to correlate our results obtained for the strength of Ti-40Nb or other heavily stabilised β alloys manufactured and tested using similar approaches to ours. For binary TiNb alloys, once the alloy is fully stabilised at room temperature, strength lowers with respect to α'' martensitic alloys but does not differ much from α' martensitic single phase [8]. In view of that, our results for Ti-40Nb match the expected trend. On the other hand, results found in literature for Ti-10Sn display discordant trends; Hsu et al. [13] registered 1,300 MPa for a Ti-10Sn (at.%), although they did not report IMCs and their set up was in bending. Park el al. [15] registered 790±10 MPa for Ti-8.1Sn (at.%) while reporting the presence of IMCs. It is difficult to assess how the presence of IMCs may affect the elastic failure mode in this alloy, and whether it is hardening strengthening due to the coherent α' superstructure or it is the presence of α'' phase that provides a hardening effect due to grain refinement (i.e. the size of the α'' grains can reach two orders of magnitude smaller than β grains). This has been reported in other studies in which the strength of TiNbSn ternary alloys increases with the presence of α'' phase [18], and our results for strength value of the ternary alloy fall in line with the results from that study.

4.5. *In vitro* studies: cytotoxicity, proliferation and metabolic activity

Cytotoxicity and proliferation studies on cells grown in direct or non-direct contact using negative controls for qualitative comparison as well as the Toluidine blue staining assay

informed that none of the alloys were toxic and, on the contrary, confirmed an active mitotic behaviour.

The discussion of the albumin protein absorption results is considered alongside those of the surface characterisation (i.e. roughness and contact angle when the medium used was PBS) and electrical resistance. It was expected that protein adsorption, the first attachment phenomenon on the substrate's surface after exposure to a biological environment, would correlate to surface hydrophilicity. Albumin is highly abundant in cellular plasma and its adsorption is representative of a large proportion of plasma proteins. It has been widely reported that albumin adsorption is negatively correlated with hydrophilicity [43] due to its negative net charge at the pH value in these conditions (7-7.3) [44] and positively correlated to roughness [45]. In this study however, c.p.Ti surfaces displayed a large protein concentration despite their low contact angle and their negatively charged (i.e. Lewis acidic) sites [46]. On the contrary and despite a contact angle very close to that of c.p.Ti, Ti-10Nb-5Sn presented the lowest levels of albumin attachment even when the surface was roughest. This indicated that hydrophilicity and surface roughness are not the only mechanisms in protein attachment on the alloys surface, as reviewed in [23]. The results in the albumin adsorption after 1 h and after 24 h obtained from the four compositions indicate that there are two types of adsorption kinetics at play. The quantification of protein absorbed by c.p.Ti was the highest amount, followed by Ti-40Nb. This result is in agreement with what has been reported in literature, that TiO_2 adsorbs more albumin than TiO_2-Nb_2O_5 surfaces [25]. C.p.Ti and Ti-40Nb albumin adsorption results after 1 h showed no significant variation after 24 h, compared to the other alloys (p *value* < 0.05). This leads to the conclusion that most binding sites available were saturated within 1 h, forming a conformal steady monolayer. On the contrary, Ti-10Sn and Ti-10Nb-5Sn, both containing SnO_x on the outermost layer, showed different adsorption kinetics. The lower degree of absorption after 1 h with a significant increase of albumin adsorption after 24 h indicates that while an initial monolayer of protein was formed, it reorganised in the subsequent hours so other protein (multi-)layers could be adsorbed. Incidentally the presence of SnO_x and Nb_xO_x decreased electrical resistance values of the alloys, which further indicates that complex electrochemistry on the cell/alloy interface may be responsible for the kinetic activity on the Sn-containing alloys *versus* c.p.Ti and Ti-40Nb .

The quantitative study of cell metabolic activity by measurement of glucose intake and lactate release over 12 days indicated that the alloys support cell growth and proliferation (Figure 10). The pre-osteoblasts consumed glucose, i.e. their main energy source, at a steadily increasing exponential rate over the duration of the study, with Ti-40Nb, Ti-10Sn and Ti-10Nb-5Sn displaying an enhanced consumption compared to the c.p.Ti (Figure 10a,c). Ti-

10Nb-5Sn presented a larger rate at day 2, probably due to its wettability, followed by Ti-40Nb and Ti-10Sn at day 4, statistically significant when compared to c.p.Ti. This is symptomatic of a larger osteoblastic proliferation in alloys which contained Nb and Sn elements. This more active mitotic behaviour is in agreement with other osteoblastic proliferation studies reported on binary Ti-Nb [46, 47] and ternary Ti-Nb-Sn systems [48].

The sigmoidal pattern of the release of lactate throughout the study (Figure 10b,d) from the cells cultured on c.p.Ti and Ti-40Nb is different to that displayed by the control (PS). Those of the Ti-10Sn and Ti-10Nb-5Sn were truly exponential. More specifically, the Sn-containing alloys presented an increased lactate release beyond day 6 compared to those of the c.p.Ti, Ti-40Nb and control. Recent studies have shown that glycolysis is the major metabolic pathway preferred by pre-osteoblasts [49] to meet their ATP (i.e. energy generation) demand during differentiation and, since lactate is the end-product of glycolysis, an increase in lactate would signal a change in the preferred energetic pathway for pre-osteoblasts cultured on Sn-containing alloys. No differences in DNA concentration on the alloys were found at day 12, confirming that the differences in glucose intake and/or lactate released were independent from cell numbers at this stage of proliferation (Figure 11). At day 12 Ti-10Nb-5Sn yielded the largest rate of glucose consumption and lactate release. There is a statistical difference between Ti-10Sn and Ti-40Nb, but when comparing Ti-10Nb-5Sn to Ti-10Sn, it falls short from statistical significance using the t-test.

Although the mechanism is not fully elucidated, it has been hypothesised that surface charge plays a role in the stimulation of cell adhesion and growth *versus* cell differentiation. Positively charged (i.e. the equivalent of Lewis acid because there is a positive shift in the surface zeta potential compared to the TiO_2) sites such as Nb_2O_5 (due to the highly polarised NbO_4 tetrahedra [50]) stimulated the initial adhesion and growth of osteosarcoma cells on Ti-37Nb (wt.%) [46], and an accelerated adhesion and differentiation was observed for human mesenchymal stromal cells in Ti-40Nb (wt.%) [51]. In this study, oxygen deficient tin oxide sites (SnO_x, $1<x<2$, as per Figure 4c) were present and may have manifested themselves also as positively charged Lewis acids sites, with Sn^{2+} cations showing higher polarisability and stronger Lewis acidity compared to Sn^{4+}[52]. It is hypothesised that their presence incurred a positive shift in the zeta potential of mixed oxide layers containing SnO_x, such as in the cases of Ti-10Sn and Ti-10Nb-5Sn, which sustained an accelerated mechanism of proliferation. To the best of the authors' knowledge, no *in vitro* studies on binary TiSn alloys used for bioengineering applications have been reported that could be used for comparison purposes.

Furthermore, the duplex-phase alloy Ti-10Nb-5Sn, which contains Nb-enriched β and Sn-enriched α'' producing a inhomogeneous surface chemistry and with localised changes in microhardness (Figure 6) and electrical resistance (Table 2), could provoke enhanced metabolic behaviour and interactions between the cells attached. We hypothesise that such a complex multi-component chemically-inhomogeneous oxide layer derived from coexisting phases, may have created preferential areas of local surface charge (i.e. TiO_2 negatively charged [46] and Nb_2O_5, SnO_x positively charged) for the cells to attach, migrate, proliferate or differentiate and hence the large variability in the metabolic activity of this particular alloy.

5. Conclusions

Binary Ti-40Nb, Ti-10Sn and ternary Ti-10Nb-5Sn (at.%) alloys were designed and manufactured to be exemplars of different titanium phases (i.e. hcp α, martensite lath-like hexagonal α' and needle-like orthogonal α'', and β grains), confirmed via EBSD, EDX and XRD assessment. Surface analyses allowed characterisation of their oxide components, predominantly Ti_xO_x with the additions of Nb_xO_x in Ti-40Nb, SnO_x in Ti-10Sn and both in Ti-10Nb-5Sn, which conferred the ternary alloy with peculiar wetting and electrical resistance properties. Their mechanical performance followed the microhardness hierarchy: c.p.Ti<Ti-40Nb<Ti-10Nb-5Sn<Ti-10Sn, although the ternary alloy exhibited a marked spread of results due to the heterogeneity in the $\beta + \alpha''$ duplex-phase. The decreasing elastic order was $E_{c.p.Ti}>E_{Ti\text{-}40Nb}>E_{Ti\text{-}10Sn}>E_{Ti\text{-}10Nb\text{-}5Sn}$, demonstrating the solid solution strengthening in the stabilised β phase Ti-40Nb alloy, and the plasticising effect of the Sn addition. The yield strength followed the order: $\sigma_{c.p.Ti}<\sigma_{Ti\text{-}10Sn}\approx\sigma_{Ti\text{-}40Nb}<\sigma_{Ti\text{-}10Nb\text{-}5Sn}$, which positioned the ternary alloy as a promising bulk material to mimic bone mechanical properties with the largest strength to Young's modulus ratio as well as the largest strain at yield amongst all the alloys in the study. While no cytotoxicity to the pre-osteoblasts was confirmed in all the alloys and all sustained fully confluent cell colonies over 12 days, those containing Sn in their composition displayed an enhanced performance in cell metabolic activity based on their increased fuel utilisation during the 12-day *in vitro* study, due to, we hypothesise, inhomogeneity in the surface charge and surface oxide composition derived from coexisting titanium allotropic phases.

Acknowledgements

Financial support from EPSRC under grant reference EP/P027482/1 is gratefully acknowledged. The Loughborough Materials Characterisation Centre and Dr Y.Y. Tse have supported materials characterisation tasks. The Centre for Biological Engineering at Loughborough University have assisted with metabolic studies.

Conflict of interests

None

Author contributions

CTS: conceptualisation, data curation, formal analysis, methodology, funding acquisition, writing original and revised draft. JW: data curation, formal analysis, visualisation, writing original draft; MN: data curation, formal analysis, visualisation, writing original draft; LZ: data curation, writing original draft; PPC: methodology, funding acquisition, supervision, writing original and revised draft.

References

[1] G. Ryan, A. Pandit, D.P. Apatsidis, Fabrication methods of porous metals for use in orthopaedic applications, Biomaterials 27(13) (2006) 2651-2670.
[2] T.-K. Jung, S. Semboshi, N. Masahashi, S. Hanada, Mechanical properties and microstructures of β Ti–25Nb–11Sn ternary alloy for biomedical applications, Materials Science and Engineering: C 33(3) (2013) 1629-1635.
[3] H. Matsumoto, S. Watanabe, S. Hanada, Beta TiNbSn Alloys with Low Young’s Modulus and High Strength, MATERIALS TRANSACTIONS 46(5) (2005) 1070-1078.
[4] D. Kuroda, M. Niinomi, M. Morinaga, Y. Kato, T. Yashiro, Design and mechanical properties of new β type titanium alloys for implant materials, Materials Science and Engineering: A 243(1) (1998) 244-249.
[5] T. Ozaki, H. Matsumoto, S. Watanabe, S. Hanada, Beta Ti Alloys with Low Young's Modulus, MATERIALS TRANSACTIONS 45(8) (2004) 2776-2779.
[6] H.Y. Kim, Y. Ikehara, J.I. Kim, H. Hosoda, S. Miyazaki, Martensitic transformation, shape memory effect and superelasticity of Ti–Nb binary alloys, Acta Materialia 54(9) (2006) 2419-2429.
[7] R. Karre, M.K. Niranjan, S.R. Dey, First principles theoretical investigations of low Young's modulus beta Ti–Nb and Ti–Nb–Zr alloys compositions for biomedical applications, Materials Science and Engineering: C 50 (2015) 52-58.
[8] Y.-H. Hon, J.-Y. Wang, Y.-N. Pan, Composition/Phase Structure and Properties of Titanium-Niobium Alloys, MATERIALS TRANSACTIONS 44(11) (2003) 2384-2390.
[9] J.J. Gutiérrez Moreno, M. Bönisch, N.T. Panagiotopoulos, M. Calin, D.G. Papageorgiou, A. Gebert, J. Eckert, G.A. Evangelakis, C.E. Lekka, Ab-initio and experimental study of phase stability of Ti-Nb alloys, Journal of Alloys and Compounds 696 (2017) 481-489.
[10] Y. Guo, K. Georgarakis, Y. Yokoyama, A.R. Yavari, On the mechanical properties of TiNb based alloys, Journal of Alloys and Compounds 571 (2013) 25-30.
[11] M. Bönisch, M. Calin, T. Waitz, A. Panigrahi, M. Zehetbauer, A. Gebert, W. Skrotzki, J. Eckert, Thermal stability and phase transformations of martensitic Ti-Nb alloys, Sci Technol Adv Mater 14(5) (2013) 055004-055004.
[12] S. Banumathy, R.K. Mandal, A.K. Singh, Structure of orthorhombic martensitic phase in binary Ti–Nb alloys, J Appl Phys 106(9) (2009) 093518.
[13] H.-C. Hsu, S.-C. Wu, Y.-S. Hong, W.-F. Ho, Mechanical properties and deformation behavior of as-cast Ti–Sn alloys, Journal of Alloys and Compounds 479(1) (2009) 390-394.
[14] H.-C. Hsu, H.-C. Lin, S.-C. Wu, Y.-S. Hong, W.-F. Ho, Microstructure and grindability of as-cast Ti–Sn alloys, Journal of Materials Science 45(7) (2010) 1830-1836.
[15] E.M. Park, C.H. Lee, J.M. Park, J.H. Han, G.A. Song, J.T. Kim, S.H. Hong, J.Y. Park, Y. Seo, N.S. Lee, K.B. Kim, Heterogeneous duplex structured Ti–Sn–Mo alloys with high strength and large plastic deformability, Journal of Alloys and Compounds 574 (2013) 546-551.
[16] C.R. Wong, R.L. Fleischer, Low frequency damping and ultrasonic attenuation in Ti3Sn-based alloys, Journal of Materials Research 9(6) (2011) 1441-1448.
[17] O.V. Vdovychenko, M.V. Bulanova, Y.V. Fartushna, A.A. Shcheretsky, Dynamic mechanical behavior of intermetallic Ti3Sn, Scripta Materialia 62(10) (2010) 758-761.

[18] H.-C. Hsu, S.-C. Wu, S.-K. Hsu, J.-Y. Syu, W.-F. Ho, The structure and mechanical properties of as-cast Ti–25Nb–xSn alloys for biomedical applications, Materials Science and Engineering: A 568 (2013) 1-7.
[19] P.E.L. Moraes, R.J. Contieri, E.S.N. Lopes, A. Robin, R. Caram, Effects of Sn addition on the microstructure, mechanical properties and corrosion behavior of Ti–Nb–Sn alloys, Materials Characterization 96 (2014) 273-281.
[20] F. Nozoe, H. Matsumoto, T.K. Jung, S. Watanabe, T. Saburi, S. Hanada, Effect of Low Temperature Aging on Superelastic Behavior in Biocompatible β TiNbSn Alloy, MATERIALS TRANSACTIONS 48(11) (2007) 3007-3013.
[21] P. Li, X. Ma, D. Wang, H. Zhang, Microstructural and Mechanical Properties of β-Type Ti–Nb–Sn Biomedical Alloys with Low Elastic Modulus, Metals 9(6) (2019) 712.
[22] Y.-H. Song, M.-K. Kim, E.-J. Park, H.-J. Song, K.J. Anusavice, Y.-J. Park, Cytotoxicity of alloying elements and experimental titanium alloys by WST-1 and agar overlay tests, Dental Materials 30(9) (2014) 977-983.
[23] P. Silva-Bermudez, S.E. Rodil, An overview of protein adsorption on metal oxide coatings for biomedical implants, Surface and Coatings Technology 233 (2013) 147-158.
[24] E. Eisenbarth, D. Velten, M. Müller, R. Thull, J. Breme, Nanostructured niobium oxide coatings influence osteoblast adhesion, Journal of Biomedical Materials Research Part A 79A(1) (2006) 166-175.
[25] T.M. Byrne, L. Lohstreter, M.J. Filiaggi, Z. Bai, J.R. Dahn, Quantifying protein adsorption on combinatorially sputtered Al-, Nb-, Ta- and Ti-containing films with electron microprobe and spectroscopic ellipsometry, Surface Science 603(7) (2009) 992-1001.
[26] C. Torres-Sanchez, F.R.A. Al Mushref, M. Norrito, K. Yendall, Y. Liu, P.P. Conway, The effect of pore size and porosity on mechanical properties and biological response of porous titanium scaffolds, Materials Science and Engineering: C 77 (2017) 219-228.
[27] Y.-J. Park, Y.-H. Song, J.-H. An, H.-J. Song, K.J. Anusavice, Cytocompatibility of pure metals and experimental binary titanium alloys for implant materials, Journal of Dentistry 41(12) (2013) 1251-1258.
[28] J. Małecka, Investigation of the Oxidation Behavior of Orthorhombic Ti2AlNb Alloy, Journal of Materials Engineering and Performance 24(5) (2015) 1834-1840.
[29] Y. Duan, N. Fu, Q. Liu, Y. Fang, X. Zhou, J. Zhang, Y. Lin, Sn-Doped TiO2 Photoanode for Dye-Sensitized Solar Cells, The Journal of Physical Chemistry C 116(16) (2012) 8888-8893.
[30] J. Wang, G.D. Wilcox, R.J. Mortimer, C. Liu, M.A. Ashworth, Electrodeposition and Characterization of Nanocrystalline Ni-NbOx Composite Coatings from Glycol-based Electrolytes for High Temperature Electronics Packaging, Journal of The Electrochemical Society 161(9) (2014) D395-D404.
[31] J. Wang, G. Chen, F. Sun, Z. Zhou, Z.-Q. Liu, C. Liu, Combined effects of surface oxidation and interfacial intermetallic compound growth on solderability degradation of electrodeposited tin thin films on copper substrate due to isothermal ageing, Corrosion Science 139 (2018) 383-394.
[32] J.F. Moulder, Chastain, J. and King, R.C., Handbook of X-Ray Photoelectron Spectroscopy: A Reference Book of Standard Spectra for Identification and Interpretation of XPS Data, Physical Electronics Division, Perkin-Elmer Corp., Eden Prairie, Minn, USA, 1995.
[33] H. Gamsjäger, T. Gajda, J. Sangster, S.K. Saxena, W. Voigt, J. Perrone, Chemical Thermodynamics of Tin – Volume 12, 2012.
[34] K. Anselme, P. Linez, M. Bigerelle, D. Le Maguer, A. Le Maguer, P. Hardouin, H.F. Hildebrand, A. Iost, J.M. Leroy, The relative influence of the topography and chemistry of TiAl6V4 surfaces on osteoblastic cell behaviour, Biomaterials 21(15) (2000) 1567-1577.
[35] M. Ball, D.M. Grant, W.J. Lo, C.A. Scotchford, The effect of different surface morphology and roughness on osteoblast‐like cells, Journal of Biomedical Materials Research Part A 86A(3) (2008) 637-647.

[36] D. Photiou, N.T. Panagiotopoulos, L. Koutsokeras, G.A. Evangelakis, G. Constantinides, Microstructure and nanomechanical properties of magnetron sputtered Ti−Nb films, Surface and Coatings Technology 302 (2016) 310-319.
[37] D.C. Zhang, S. Yang, M. Wei, Y.F. Mao, C.G. Tan, J.G. Lin, Effect of Sn addition on the microstructure and superelasticity in Ti–Nb–Mo–Sn Alloys, Journal of the Mechanical Behavior of Biomedical Materials 13 (2012) 156-165.
[38] W.F. Ho, C.P. Ju, J.H. Chern Lin, Structure and properties of cast binary Ti–Mo alloys, Biomaterials 20(22) (1999) 2115-2122.
[39] E.P. Utomo, I. Kartika, A. Anawati, Effect of Sn on mechanical hardness of as-cast Ti-Nb-Sn alloys, AIP Conference Proceedings 1964(1) (2018) 020046.
[40] M. Bulanova, Y. Podrezov, Y. Fartushna, Phase composition, structure and mechanical properties of Ti–Dy–Si–Sn alloys, Intermetallics 14(4) (2006) 435-443.
[41] D.C. Zhang, Y.F. Mao, Y.L. Li, J.J. Li, M. Yuan, J.G. Lin, Effect of ternary alloying elements on microstructure and superelastictity of Ti–Nb alloys, Materials Science and Engineering: A 559 (2013) 706-710.
[42] Y. Mantani, K. Kudou, Effect of plastic deformation on material properties and martensite structures in Ti–Nb alloys, Journal of Alloys and Compounds 577 (2013) S448-S452.
[43] R.L. Williams, D.F. Williams, Albumin adsorption on metal surfaces, Biomaterials 9(3) (1988) 206-212.
[44] K. Baler, O.A. Martin, M.A. Carignano, G.A. Ameer, J.A. Vila, I. Szleifer, Electrostatic Unfolding and Interactions of Albumin Driven by pH Changes: A Molecular Dynamics Study, The Journal of Physical Chemistry B 118(4) (2014) 921-930.
[45] A.C. De Luca, M. Zink, A. Weidt, S.G. Mayr, A.E. Markaki, Effect of microgrooved surface topography on osteoblast maturation and protein adsorption, Journal of Biomedical Materials Research Part A 103(8) (2015) 2689-2700.
[46] M. Vandrovcova, I. Jirka, K. Novotna, V. Lisa, O. Frank, Z. Kolska, V. Stary, L. Bacakova, Interaction of Human Osteoblast-Like Saos-2 and MG-63 Cells with Thermally Oxidized Surfaces of a Titanium-Niobium Alloy, PLOS ONE 9(6) (2014) e100475.
[47] A. Ochsenbein, F. Chai, S. Winter, M. Traisnel, J. Breme, H.F. Hildebrand, Osteoblast responses to different oxide coatings produced by the sol–gel process on titanium substrates, Acta Biomaterialia 4(5) (2008) 1506-1517.
[48] C.Y. Acevedo-Morantes, R.A. Irizarry-Ortiz, P.G. Caceres-Valencia, S.P. Singh, J.E. Ramirez-Vick, Combinatorial growth of oxide nanoscaffolds and its influence in osteoblast cell adhesion, J Appl Phys 111(10) (2012) 102810-1028107.
[49] W.-C. Lee, A.R. Guntur, F. Long, C.J. Rosen, Energy Metabolism of the Osteoblast: Implications for Osteoporosis, Endocr Rev 38(3) (2017) 255-266.
[50] K. Nakajima, Y. Baba, R. Noma, M. Kitano, J. N. Kondo, S. Hayashi, M. Hara, Nb2O5·nH2O as a Heterogeneous Catalyst with Water-Tolerant Lewis Acid Sites, Journal of the American Chemical Society 133(12) (2011) 4224-4227.
[51] A. Helth, P.F. Gostin, S. Oswald, H. Wendrock, U. Wolff, U. Hempel, S. Arnhold, M. Calin, J. Eckert, A. Gebert, Chemical nanoroughening of Ti40Nb surfaces and its effect on human mesenchymal stromal cell response, Journal of Biomedical Materials Research Part B: Applied Biomaterials 102(1) (2014) 31-41.
[52] M.W. Abee, D.F. Cox, NH3 chemisorption on stoichiometric and oxygen-deficient SnO2(110) surfaces, Surface Science 520(1) (2002) 65-77.

Journal Pre-proof

Declaration of interests

☒ The authors declare that they have no known competing financial interests or personal relationships that could have appeared to influence the work reported in this paper.

☐The authors declare the following financial interests/personal relationships which may be considered as potential competing interests:

No conflict of interests

Journal Pre-proof

Graphical abstract

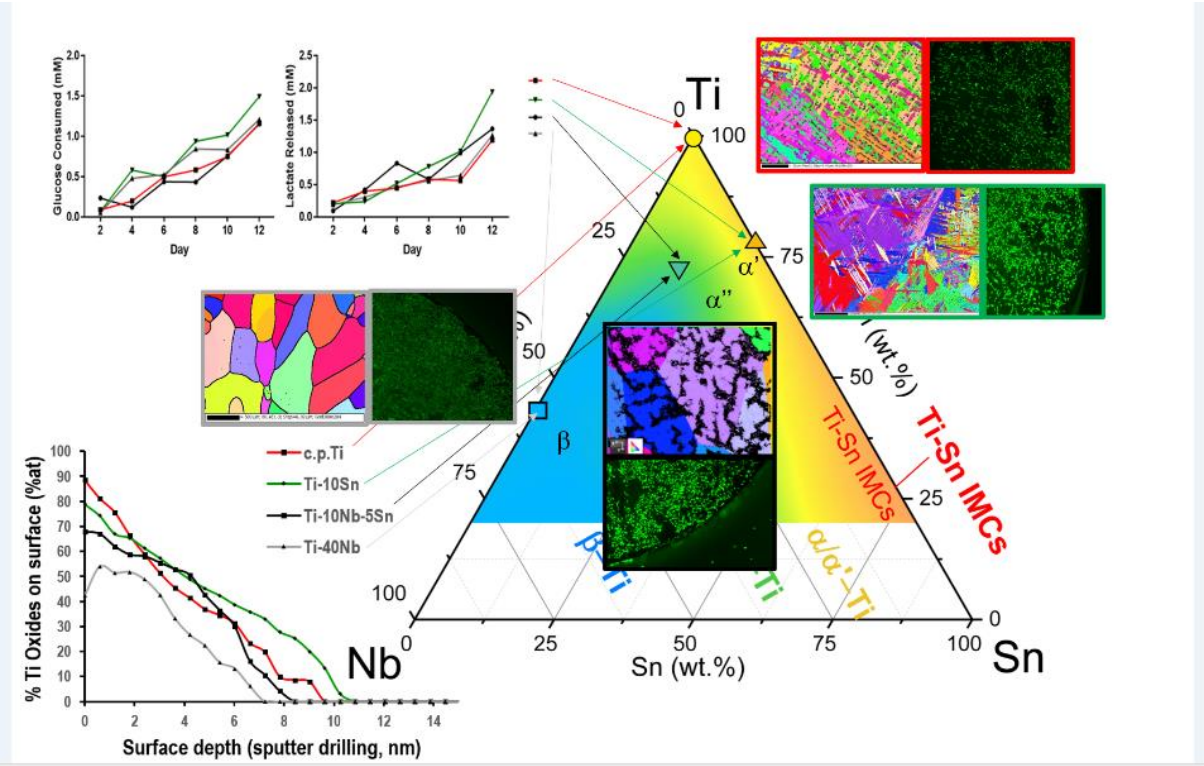

Highlights:

- Ti10Nb5Sn has a duplex β + α'' phase displaying largest microhardness and strain at yield
- Ti10Nb5Sn alloy had the largest strength to stiffness ratio (vs Ti, TiNb, TiSn)
- Sn-alloys showed changes in cellular behaviour at day 6, signalling a different pathway
- Sn-containing alloys displayed more metabolite content at day 12 vs Ti-only and TiNb alloys
- Sn-containing alloys oxide surface complexity (chemistry and electrical) suspected to rule their different behaviour